

Highly Resolved and Robust Dynamic X-Ray Imaging Using Perovskite Glass-Ceramic Scintillator with Reduced Light Scattering

Wenbo Ma, Tingming Jiang, Ze Yang, Hao Zhang, Yirong Su, Zeng Chen, Xinya Chen, Yaoguang Ma, Wenjuan Zhu, Xue Yu, Haiming Zhu, Jianbei Qiu, Xu Liu, Xuhui Xu,* and Yang (Michael) Yang*

All-inorganic perovskite quantum dots (QDs) CsPbX_3 ($X = \text{Cl, Br, and I}$) have recently emerged as a new promising class of X-ray scintillators. However, the instability of perovskite QDs and the strong optical scattering of the thick opaque QD scintillator film impeded it to realize high-quality and robust X-ray image. Herein, the europium (Eu) doped CsPbBr_3 QDs are in situ grown inside transparent amorphous matrix to form glass-ceramic (GC) scintillator with glass phase serving as both matrix and encapsulation for the perovskite QD scintillators. The small amount of Eu dopant optimizes the crystallization of CsPbBr_3 QDs and makes their distribution more uniform in the glass matrix, which can significantly reduce the light scattering and also enhance the photoluminescence emission of CsPbBr_3 QDs. As a result, a remarkably high spatial resolution of 15.0 lp mm^{-1} is realized thanks to the reduced light scattering, which is so far a record resolution for perovskite scintillator based X-ray imaging, and the scintillation stability is also significantly improved compared to the bare perovskite QD scintillators. Those results provide an effective platform particularly for the emerging perovskite nanocrystal scintillators to reduce light scattering and improve radiation hardness.

1) direct conversion of X-ray photons into electrical signal; 2) indirect conversion by using scintillators to convert X-ray photons to visible photons first and then be detected by photodiode. In the past few years, perovskite semiconductors have demonstrated great potentials in direct X-ray detection due to their exceptional properties such as large X-ray attenuation coefficient, large mobility-lifetime product ($\mu\tau$), and low-cost solution process.^[10–18] Recently, all-inorganic CsPbX_3 ($X = \text{Cl, Br, I}$) perovskite scintillators have been explored due to their large X-ray absorption efficiency, intense radioluminescence (RL), low X-ray detection limit, and fast light decay,^[1–4,17–19] which make them highly competitive to the commercial scintillators, for example, CsI:TI ^[20] and LuAG:Ce based scintillators.^[21] In addition, perovskite-like metal halides featuring self-trapped exciton emissions have revealed good X-ray scintillation with large Stokes shift and high light yield.^[22,23]

One advantage of inorganic perovskite as scintillator is that there is no need to grow as big crystals as many conventional scintillator to obtain good scintillation yield, in contrast, the scintillation of CsPbBr_3 nanocrystal is several orders of magnitudes stronger than CsPbBr_3 single crystal.^[1] However,


X-ray has been widely used in probing the inside information of condensed matter subjects non-destructively, enabling broad applications in safety inspection, medical radiography, defect inspection, etc.^[1–9] There are two approaches to detect X-ray:

scintillator is that there is no need to grow as big crystals as many conventional scintillator to obtain good scintillation yield, in contrast, the scintillation of CsPbBr_3 nanocrystal is several orders of magnitudes stronger than CsPbBr_3 single crystal.^[1] However,

W. Ma, Dr. T. Jiang, Y. Su, X. Chen, Prof. Y. Ma, Dr. W. Zhu, Prof. X. Liu, Prof. Y. (Michael) Yang
State Key Laboratory of Modern Optical Instrumentation
College of Optical Science and Engineering
International Research Center for Advanced Photonics
Key Laboratory of Excited State Materials of Zhejiang Province
Zhejiang University
Hangzhou, Zhejiang 310027, China
E-mail: yangyang15@zju.edu.cn

Z. Yang, H. Zhang, Prof. X. Yu, Prof. J. Qiu, Prof. X. Xu
Faculty of Material Science and Engineering
Kunming University of Science and Technology
Kunming, Yunnan 650000, China
E-mail: xuxuh07@kust.edu.cn

Z. Chen, Prof. H. Zhu
Center for Chemistry of High-Performance and Novel Materials
Department of Chemistry
Zhejiang University
Hangzhou, Zhejiang 310027, China

 The ORCID identification number(s) for the author(s) of this article can be found under <https://doi.org/10.1002/advs.202003728>

© 2021 The Authors. Advanced Science published by Wiley-VCH GmbH. This is an open access article under the terms of the Creative Commons Attribution License, which permits use, distribution and reproduction in any medium, provided the original work is properly cited.

DOI: 10.1002/advs.202003728

this unique feature also brings dark sides. First, it requires the perovskite nanocrystal film to be at least several hundred micrometers to ensure sufficient X-ray absorption, such thick film is opaque and the light scattering severely affects the imaging resolution. Second, the stability issue could become even more severe when perovskite crystals shrink to nanometer size due to the massively increased surface/bulk ratio. In addition, the water soluble lead of perovskite nanocrystal is always a risk to human and environment.^[13,24] Growing QDs inside inorganic glass has been proven as an effective strategy to prevent the degradation and enhance the environmental stability of II–VI and IV–VI QDs,^[25–28] as well as CsPbX₃ QDs showing applications in white LED,^[29–36] lasing,^[36] and 3D laser printing.^[37] Here, to resolve those above concerns, we in situ grew inorganic perovskite QDs inside transparent and robust matrix as a glass-ceramic (GC) scintillator, which is inexpensive to fabricate and can be easily scaled up. The incorporation of small amount of Eu improves the crystallinity of CsPbBr₃ QDs and alters its size distribution, which further enhances the scintillator performance in terms of spatial resolution and light yield. Finally, our CsPbBr₃:Eu GC scintillator with significantly reduced light scattering enables X-ray images with high spatial resolution of 15 lp mm⁻¹, even superior to commercial CsI (TI) scintillator and delivers impressive stability under continuous X-ray illumination and thermal stressing in humid air.

The CsPbBr₃ QDs grown in glass matrix was prepared from the transparent precursor glass (PG) by melt-quenching method, whose XRD pattern of PG (Figure 1a) showed diffuse hump without any diffraction peaks due to its amorphous character. Subsequently the PG was annealed at 500 °C and the CsPbBr₃ QDs were precipitated inside it, as evidenced by the XRD peaks (Figure 1a) that are well indexed to pure CsPbBr₃ cubic phase (JCPDS No. 54–0752). TEM bright field image of CsPbBr₃ GC (Figure 1b) presents dark spherical CsPbBr₃ nanocrystals embedded in glass with average diameter of ≈11 nm. And high-resolution TEM image (Figure 1c) shows clear lattice fringe with interplanar distance between two adjacent crystal planes of ≈0.348 nm, in agreement with the (110) plane of cubic CsPbBr₃ crystal. Interestingly, the nanocrystals shrink to the typical size of quantum dots (≈5 nm) with the incorporation of Eu, and the size distribution is more uniform shown in Figure 1d. We reason that the doped Eu³⁺ likely acts as a nucleation agent which can promote rapid growth and precipitation of CsPbBr₃, thus decrease the crystal size and improve the uniformity. In order to conform this, we monitored the in situ growth of CsPbBr₃ QDs induced by high-energy electron beam inside PG as shown in Figures S1 and S2, Supporting Information. The TEM images demonstrate the CsPbBr₃ QDs are crystallized more rapidly, easily, and uniformly inside Eu doped PG. Since the thickness of the GC is about 2 mm, the perovskite loading among glass is determined to be ≈116 μm based on molar ratio of source materials and their corresponding density, which is similar to the reference nanocrystal film of ≈100 μm thickness. Since Rayleigh scattering intensity is proportional to d^6 (diameter of the dots), the light scattering for the Eu doped CsPbBr₃ QDs GC, with optimized doping ratio of 1.5% (Figure 1e) can be significantly eliminated, which ultimately translates to reduced signal crosstalk in photodiode array and therefore improve the image resolution. Figure 1f presents the photographs of CsPbBr₃ GC with and without Eu³⁺ dopant

as well as conventional CsPbBr₃ nanocrystal film, demonstrating distinctly improved transparency for CsPbBr₃:Eu GC visually, mainly because of the reduced scattering rather than the difference of absorption. We applied Eu doping strategy to grow other perovskite QDs (CsPbCl₃ and CsPbI₃) in the same glass matrix and found the sizes of perovskite QDs also uniformly distributed in the matrix as shown in Figure S1, Supporting Information, which demonstrates the effectiveness of this approach.

X-ray photoelectron spectroscopy (XPS) measurements were carried out to study the doping effect of Eu³⁺ ions. The binding energy of Pb 4f_{7/2} shifts from 139.2 eV for CsPbBr₃ GC to 138.73 eV for CsPbBr₃:Eu GC shown in Figure 1g, which may originate from the increased electron density around Pb²⁺ after Eu³⁺ doping, since stronger bonding interaction between Eu³⁺ and Br⁻ may result in less electron donation from Pb²⁺ to Br⁻ and thereby increase electron density around Pb²⁺.^[38] This result indicates Eu³⁺ ions occupy the Pb²⁺ sites in the CsPbBr₃ lattice during the CsPbBr₃ crystallization under high temperature, since the ionic radius of Pb²⁺ and Eu³⁺ are comparable (Pb²⁺: 119 pm, Eu³⁺: 95 pm). The XPS spectrum of Eu³⁺ 3d_{5/2} shown in Figure 1h with binding energy at about 1135 eV is almost symmetric and can be fitted perfectly with one gaussian-component suggesting only one chemical environment of Eu³⁺ existing either in glass matrix or in the Pb²⁺ lattice sites of CsPbBr₃ QDs. Based on the above analysis, we reason that the lightly doped Eu³⁺ (1.5%) ions are almost entirely incorporated into the CsPbBr₃ lattice. Due to the unequal charge of Pb²⁺ and Eu³⁺, the Eu²⁺ is also generated in GC as evidenced by the Eu²⁺ 3d_{5/2} spectrum with binding energy at 1125 eV (Figure 1h) in order to keep the charge neutrality.^[39,40] This phenomenon can be explained by the charge compensation model based on substitution defect mechanism^[40] giving rise to reduction of Eu³⁺ to Eu²⁺. Figure 1i shows photoluminescence (PL) spectra of CsPbBr₃:x%Eu GC as a function of Eu concentration. The PL intensity of CsPbBr₃ increases gradually as the increase of Eu content because of the promoted nucleation of CsPbBr₃ QD leading to more specially-confined dots with smaller sizes,^[41,42] also reflected by TEM observation in Figure 1b–d delivering 65% PL yield for CsPbBr₃:1.5%Eu GC. However, the characteristic Eu³⁺ emission (inset in Figure 1i) is almost suppressed but still observable. This is in contrast with some previous reports of Eu doped CsPbX₃ nanocrystal or glass ceramic, in which the emission intensity of Eu is comparable with or even stronger than that of CsPbX₃.^[32,33,38,43–45] This discrepancy is likely attributed to our excellent crystallization of CsPbBr₃ promoted by Eu dopant, which makes the band-to-band emission of CsPbBr₃ extremely strong, and thereby the Eu intensity seems barely observable. The transparent matrix also serves as inherent protection for perovskite quantum dots. As shown in Video S1, Supporting Information, the PL emission of CsPbBr₃ nanocrystal film is immediately quenched when dropped into boiling water, while our CsPbBr₃:Eu GC is barely affected, proving its toughness under extreme conditions. Besides, the toxic lead is also kept from dissolving into water with the encapsulation of glass matrix, as confirmed by the inductively coupled plasma atomic emission spectrometry (ICP-AES) measurement. (Table S1, Supporting Information). It showed that only 0.093 mg L⁻¹ of Pb²⁺ was traced in water after the CsPbBr₃:Eu GC was kept in water for 1 h, while 2.06 mg L⁻¹ of Pb²⁺ was detected for the

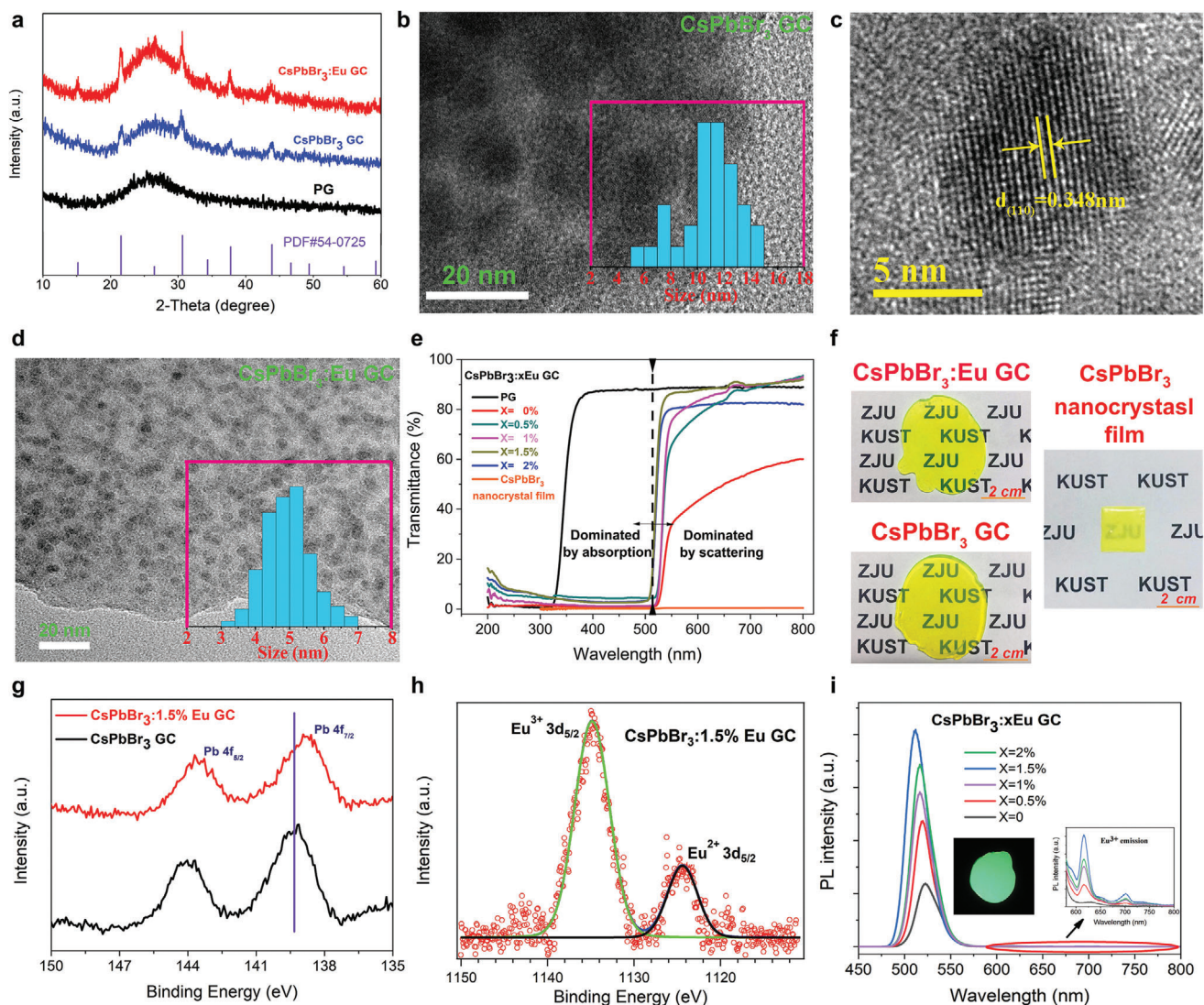


Figure 1. Fabrication and characterization of CsPbBr₃ quantum dots (QDs) inside transparent amorphous matrix. a) XRD patterns of precursor glass (PG), CsPbBr₃ QDs with and without Eu dopant in GC. b) TEM image of CsPbBr₃ QDs without Eu dopant in glass (quantum dot size distribution shown in inset). c) HRTEM image of CsPbBr₃ GC. d) TEM image of CsPbBr₃:Eu GC (quantum dot size distribution shown in inset). e) Transmittance spectra of CsPbBr₃:xEu QDs in glass as a function of Eu concentration (transmittance spectrum of PG measured as a reference). f) Photographs of CsPbBr₃ GC, CsPbBr₃:1.5%Eu GC (optimal concentration of Eu dopant) and conventional CsPbBr₃ nanocrystal film with thickness of about 100 μm (CsPbBr₃ nanocrystals and polystyrene are uniformly mixed with the ratio of 1:5). g) Pb 4f XPS spectra of CsPbBr₃ GC with and without Eu dopant. h) Eu 3d_{5/2} XPS spectrum of CsPbBr₃:1.5%Eu GC. i) Photoluminescence (PL) spectra of CsPbBr₃:xEu GC as a function of Eu concentration under 365 nm UV excitation (photograph of CsPbBr₃:1.5%Eu GC emission and enlargement of Eu³⁺ emission shown in the inset). PL spectra is measured with integrating sphere to ensure fair comparison

conventional CsPbBr₃ nanocrystal film under the same circumstance.

To access its potential as X-ray scintillator, we conducted the radioluminescence related experiments. **Figure 2a** gives the RL spectra of CsPbBr₃ GC with and without Eu dopant under X-ray excitation. The RL intensity of CsPbBr₃ GC at 530 nm enhances significantly with Eu³⁺ doping, consistent with the PL results. Different from the PL spectra, the relatively strong characteristic emissions of Eu³⁺ with peaks at 595, 616, 654, and 701 nm, which can be assigned to 5D₀ → 7F_j (j = 1, 2, 3, 4)^[46,47] transitions of Eu³⁺ ions respectively, become more distinct under X-ray excita-

tion. This feature brings an extra advantage that the overlap between RL spectra and absorption is largely reduced leading to decreased self-absorption,^[48] while the Stokes shift of mere CsPbBr₃ perovskite is very small due to its direct bandgap nature. The integrated RL intensity of CsPbBr₃:Eu GC as a function of incident X-ray dose rate is shown in Figure 2b revealing a super-linear relation, which is beneficial for obtaining good X-ray image contrast. The discrepancy between PL and RL for CsPbBr₃:Eu GC is possibly associated with the different excitation mechanism under UV and X-ray. The incident X-ray photons first interact with the heavy atoms of CsPbBr₃ via photoelectric effect and Compton

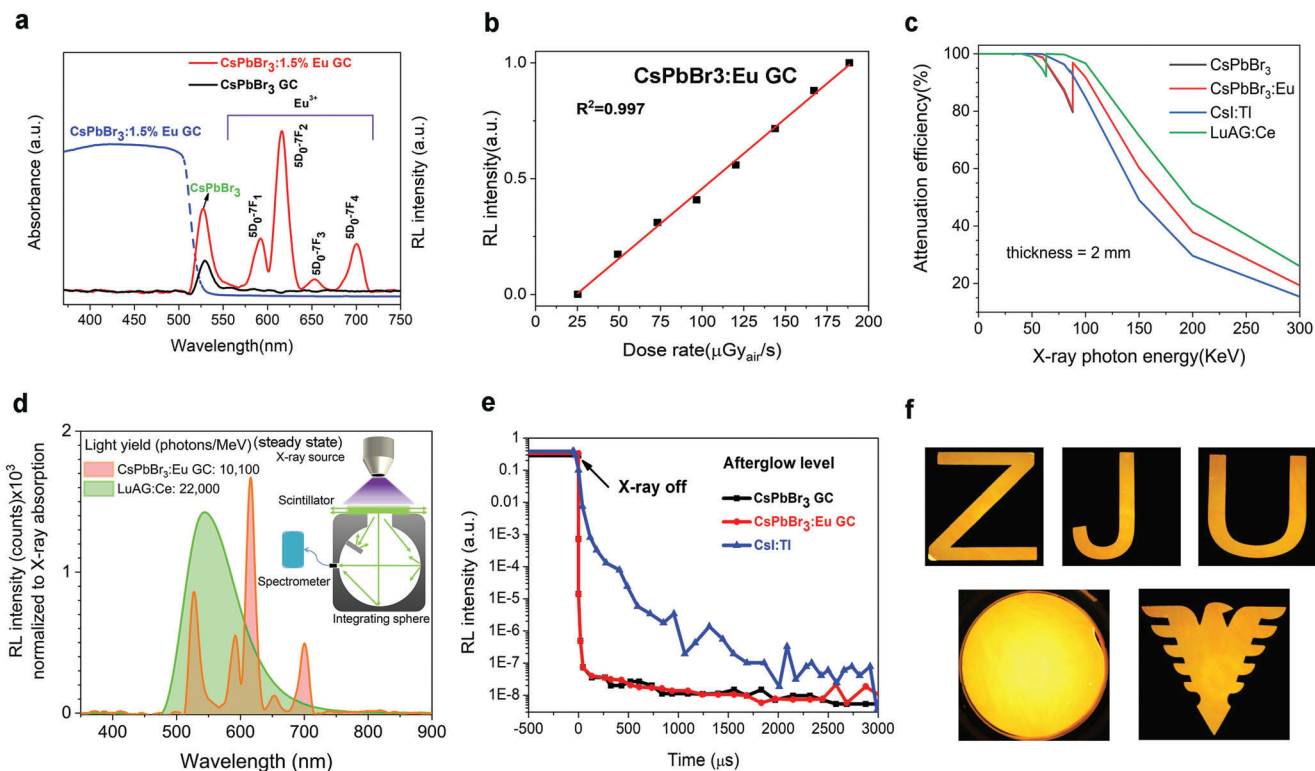


Figure 2. Characterizations of CsPbBr₃:Eu GC as X-ray scintillator. a) Radioluminescence (RL) spectra of CsPbBr₃ GC, CsPbBr₃:1.5%Eu GC (optimal concentration of Eu dopant) under X-ray excitation with a dose rate of 189 $\mu\text{Gy}_{\text{air}} \text{s}^{-1}$ at a voltage of 50 kV. The absorption spectra is also included to demonstrate the self-absorption issue. b) RL intensity dependence on X-ray irradiation. c) X-ray attenuation efficiency of CsPbBr₃ GC, CsPbBr₃:1.5%Eu GC, commercial CsI:TI, and LuAG:Ge. d) Steady-state light yield calculation of our optimized CsPbBr₃:1.5%Eu GC, commercial CsPbBr₃:1.5%Eu GC, commercial CsI:TI, and LuAG:Ge, inset figure is the measurement setup with integrating sphere. e) Afterglows of CsPbBr₃ GC scintillators with and without Eu dopant, compared with widely-used CsI:TI commercial scintillator. f) Photograph of CsPbBr₃:1.5%Eu GC under X-ray illumination (dose rate of 189 $\mu\text{Gy}_{\text{air}} \text{s}^{-1}$, voltage: 50 kV).

scattering. Note that the molar ratio of CsPbBr₃ and Eu₂O₃ (Eu³⁺ source) is $\approx 17:1.5$, thus CsPbBr₃ QDs are the major contributors of X-ray absorption as shown in Figure 2c. Once the X-ray photons are absorbed, they will be first converted to high-energy ejected electrons. These electrons with high kinetic energies move and scatter through their surrounding materials, losing energy progressively by causing other secondary electrons, and then are transported to the luminescent centers (CsPbBr₃ and Eu³⁺ ions in this case).^[1,49,50] In our case, we suppose that many of the hot and secondary electrons originated from CsPbBr₃ are captured by the Eu³⁺ luminescent centers since the Eu³⁺ are incorporated into CsPbBr₃ crystal lattice. This conjecture can be confirmed by comparing the RL intensity of reference glass sample with the same amount of 1.5%Eu and CsPbBr₃:1.5%Eu GC, in which the Eu³⁺ RL intensity is more intense than the reference glass sample as shown in Figure S4, Supporting Information. Figure 2d gives the estimation of the X-ray light yield of the perovskite glass-ceramic scintillator under steady state X-ray illumination, the reference sample was LuAG:Ce which had similar light decay constant to perovskite scintillators. It demonstrated the CsPbBr₃:1.5%Eu GC scintillator had an estimated X-ray light yield (steady-state) of 10 100 photons per MeV. The light yield describes the X-ray to photon conversion efficiency, and is considered as an internal quantum efficiency, an analogy to PL quantum yield. Hence its value significantly depends on how the

X-ray absorption is determined, which is sort of ambiguous here. Herein we treated the whole perovskite GC as the X-ray absorber although the glass matrix was non-emissive, in such a way that the value of 10 100 photons per MeV was obtained. The ultimate output light intensity depends on not only light yield but also X-ray absorption coefficient and light outcoupling efficiency. Fast light decay of perovskite scintillator is considered as one of the major advantages over the conventional scintillators.^[1–3,19] One might have the concern of whether this unique feature is still kept with Eu doping. The results in Figure 2e relieve us that the CsPbBr₃:1.5%Eu GC has almost as fast light decay as non-doped CsPbBr₃, both clearly outperforming commercial CsI:TI. The measurement was conducted with an industrial test kit in Hamamatsu scintillator department, with which the X-ray source can be immediately shut off by instantly shifting the electron beam off the metal target. The time correlated single photon counting measurement in Figure S5, Supporting Information, indicates the decay time of CsPbBr₃:1.5%Eu GC and CsPbBr₃ GC are 6.78 and 2.89 ns respectively, both in the nanosecond regime. Finally, Figure 2f shows the photographs of CsPbBr₃:Eu GC scintillations under X-ray excitation exhibiting strong and uniform emissions. Table S2, Supporting Information, illustrates the figures of merits of perovskite glass ceramic scintillator, together with previously reported perovskite scintillators and some typical commercial scintillators. Despite decades of intensive research of

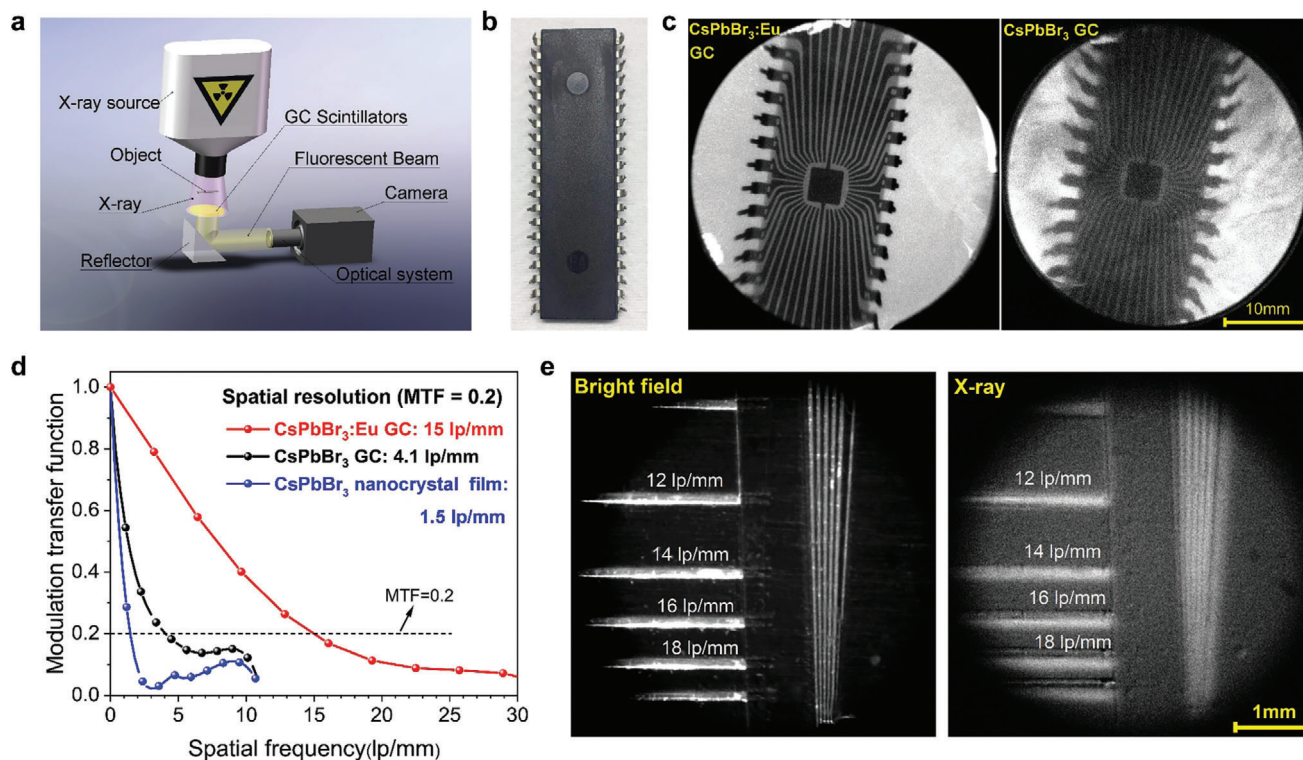


Figure 3. Spatial resolution evaluation of X-ray imaging based on three scintillators: CsPbBr₃ nanocrystal film, CsPbBr₃ GC, and CsPbBr₃:1.5%Eu GC. a) The schematic of X-ray imaging system. b) Photograph of chip A. c) X-ray images of chip A using CsPbBr₃ GC scintillators with and without Eu³⁺ doping (dose rate: 47.2 $\mu\text{Gy}_{\text{air}} \text{s}^{-1}$, voltage: 50 kV). d) Modulation transfer functions (MTF) of X-ray images obtained from CsPbBr₃ GC scintillators with and without Eu³⁺ doping, the conventional CsPbBr₃ nanocrystal film scintillator is set as reference. The image's spatial resolutions (when MTF value equals 0.2) acquired from CsPbBr₃ GC, CsPbBr₃:Eu GC, and CsPbBr₃ QDs scintillators are 15.0, 4.1, and 1.5 lp mm^{-1} , respectively. e) Bright field and X-ray image of standard X-ray resolution test pattern plate using CsPbBr₃:Eu GC scintillator (dose rate: 189 $\mu\text{Gy}_{\text{air}} \text{s}^{-1}$, voltage: 50 kV).

inorganic scintillators, there is not yet a single material that combines all the figures of merits, instead people have developed many scintillators for different applications. The perovskite GC scintillator, though not ideal, has balanced parameters of moderate light yield and fast light decay, which might be useful in some of the real applications, for example, dynamic X-ray imaging or even medical CT that requires high time resolution and high stability.

The above characterizations imply the potential of CsPbBr₃:Eu GC as scintillator for X-ray imaging. Herein, we built a homemade X-ray imaging system in **Figure 3a**, and successfully acquired X-ray images of chip A (optical photograph shown in **Figure 3b**) by using CsPbBr₃ GC without and with Eu³⁺ doping. As expected, the image quality using CsPbBr₃:Eu GC is clearly better than the one using non doped CsPbBr₃ GC, due to the enhanced RL intensity and reduced light scattering (**Figure 3c**). The X-ray image of chip B acquired by conventional CsPbBr₃ nanocrystal film reveals quite weaker image sharpness because of the strong optical crosstalk induced by light scattering (**Figure S6**, Supporting Information). The modulation transfer functions (MTF)^[51] of images obtained from CsPbBr₃ GC, CsPbBr₃:Eu GC, and CsPbBr₃ nanocrystal film have been calculated by the slanted-edge method^[52] to compare the spatial resolution (**Figure 3d**). X-ray edge images used for MTF calculation are shown in **Figure S7**, Supporting Information. The spatial resolution is

defined to be the spatial frequency (lp mm^{-1}) at $\text{MTF} = 0.2$. As a result, the image resolution with CsPbBr₃:Eu GC scintillator is 15.0 lp mm^{-1} which is much larger than 4.1 lp mm^{-1} for CsPbBr₃:GC, while conventional CsPbBr₃ nanocrystal film only gives 1.5 lp mm^{-1} . To further confirm those values, we took images of the standard X-ray resolution test pattern plate (**Figure 3e**), showing the observation limit was between ≈ 14 and 16 lp mm^{-1} , consistent with its calculated MTF value. The corresponding X-ray images of standard test pattern plate for referencing CsPbBr₃ GC and CsPbBr₃ nanocrystal film are presented in **Figure S8**, Supporting Information. It is noted that the referencing CsPbBr₃ nanocrystal film was reported with 9.8 lp mm^{-1} in the system with scintillator screen very close to the photodiode array,^[2] such that the optical crosstalk of scattered scintillation light makes minimum impact. In our case, the camera is placed away from the scintillator screen in order to increase field of view, and we should expect even better resolution if the transparent GC scintillator is attached closely to the CMOS sensor of same pixel size. Even so, this is still the highest spatial resolution for perovskite-based X-ray imaging^[1,2] to the best of our knowledge, it is even superior to 10 lp mm^{-1} of the typical commercial CsI (TI) scintillator based X-ray imaging.^[16]

The X-ray radiation stability, thermal and environmental stability of CsPbBr₃:Eu GC scintillator has been systematically investigated in terms of RL, X-ray image quality. The RL intensity

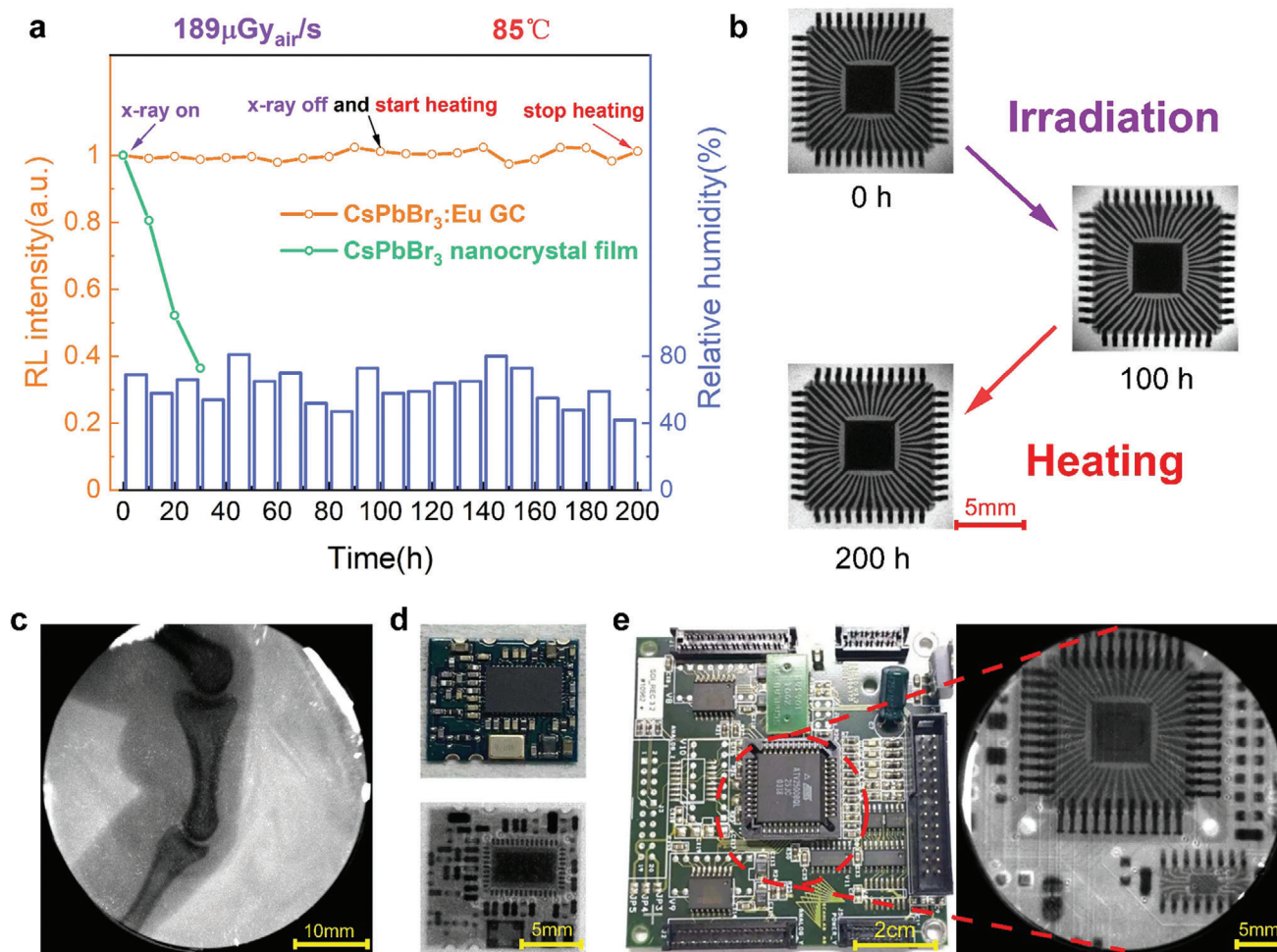


Figure 4. Stability test and X-ray imaging demos of objects of interest. a) RL intensity monitoring of CsPbBr₃:Eu GC and conventional CsPbBr₃ nanocrystal film under X-ray illumination and thermal stressing in humid air: X-ray irradiation for the initial 100 h (dose rate of $189 \mu\text{Gy}_{\text{air}} \text{ s}^{-1}$, voltage: 50 KV), and subsequently another 100 h heating under 85°C , the moisture level is recorded as well. The intensity is measured with integrating sphere. b) The X-ray images of chip B acquired at three different stages (0, 100, and 200 h). c) X-ray image of artificial finger (dose rate: $189.0 \mu\text{Gy}_{\text{air}} \text{ s}^{-1}$, voltage: 50 KV). d) Photograph of circuit board A (top) and its X-ray image (below) (dose rate: $47.2 \mu\text{Gy}_{\text{air}} \text{ s}^{-1}$, voltage: 50 KV). e) Photograph of a circuit board B (left) and X-ray image of its central part encircled by red dash lines (right) (dose rate: $47.2 \mu\text{Gy}_{\text{air}} \text{ s}^{-1}$, voltage: 50 KV).

has retained almost 100% of its initial value following continuous X-ray irradiation for 100 h and thermal annealing for another 100 h under 85°C , clearly outperforming the conventional nanocrystal film shown in **Figure 4a**. The relative humidity was also recorded every 10 h showing a humid ambient of the testing environment (RH: $\approx 40\%$ and 80%). The corresponding X-ray images of chip B was acquired at three specific timing during the aging process (0, 100, and 200 h), which gave nearly identical sharpness visually (**Figure 4b**). X-ray images of chip B obtained at every 10 h during the stability test are presented in **Figure S9**, Supporting Information. The stability tests demonstrate robustness of our CsPbBr₃:Eu GC as scintillator against harsh ambient environment (high humidity, thermal annealing) and longtime X-ray illumination. **Figure 4c** shows high-quality X-ray image of human finger with obvious biological tissue phase contrast and clear joint details benefited from the low optical crosstalk of the scintillation. **Figure 4d,e** are the X-ray images of different circuit boards with various electronic components. To access the suit-

ability of CsPbBr₃:Eu GC scintillator for the real-time X-ray imaging, a video-rate X-ray imaging of artificial bone bending (**Video S2**, Supporting Information) was made which exhibited a distinct phase contrast without ghost imaging effect. Moreover, we monitored the incubation process of a fertilized quail egg by acquiring its X-ray images during the incubation process (**Figure S10**, Supporting Information). The image obtained at the 12th day showed obvious phase contrast and a pair of wings appeared indistinctly. These X-ray imaging demos demonstrate great potential of CsPbBr₃:Eu GC scintillator for the medical or industrial X-ray imaging application.

In conclusion, we have successfully developed an Eu doped perovskite glass-ceramic scintillator to eliminate the scintillation scattering and improve operational stability. The incorporation of Eu promotes the crystallization of CsPbBr₃ QDs, and makes them distribute uniformly in the matrix. As a result, high resolution X-ray imaging of 15 lp mm^{-1} is realized. In the meanwhile, the operational and environmental stability of CsPbBr₃:Eu GC

scintillators are significantly enhanced. This approach and platform could also be applicable to other perovskite or perovskite derivative scintillators that might possess better figures of merits than CsPbBr₃ scintillators.

Supporting Information

Supporting Information is available from the Wiley Online Library or from the author.

Acknowledgements

W.M. and T.J. contributed equally to this work. The authors acknowledge the support from the National Key Research and Development Program of China (2017YFA0207700), Outstanding Youth Fund of Zhejiang Natural Science Foundation of China (LR18F050001), National Science Foundation of China (61804134), National Nature Science Foundation of China (NSFC) (61965012), Yunnan Ten Thousand Talents Plan Young & Elite Talents Project (YNWR-QNBJ-2018-295, YNWR-QNBJ-2018-325), the Excellent Youth Project of Yunnan Province Applied Basic Research Project (2019FI001).

Conflict of Interest

The authors declare no conflict of interest.

Data Availability Statement

Research data are not shared.

Keywords

perovskites, quantum dots, scintillator, spatial resolution, X-ray imaging

Received: September 30, 2020

Revised: January 31, 2021

Published online: June 2, 2021

- [1] Q. Chen, J. Wu, X. Ou, B. Huang, J. Almutlaq, A. A. Zhumekenov, X. Guan, S. Han, L. Liang, Z. Yi, J. Li, X. Xie, Y. Wang, Y. Li, D. Fan, D. B. L. Teh, A. H. All, O. F. Mohammed, O. M. Bakr, T. Wu, M. Bettinelli, H. Yang, W. Huang, X. Liu, *Nature* **2018**, *561*, 88.
- [2] J. H. Heo, D. H. Shin, J. K. Park, D. H. Kim, S. J. Lee, S. H. Im, *Adv. Mater.* **2018**, *30*, 1801743.
- [3] Y. Zhang, R. Sun, X. Ou, K. Fu, Q. Chen, Y. Ding, L. J. Xu, L. Liu, Y. Han, A. V. Malko, X. Liu, H. Yang, O. M. Bakr, H. Liu, O. F. Mohammed, *ACS Nano* **2019**, *13*, 2520.
- [4] F. Cao, D. Yu, W. Ma, X. Xu, B. Cai, Y. M. Yang, S. Liu, L. He, Y. Ke, S. Lan, K. L. Choy, H. Zeng, *ACS Nano* **2019**, *14*, 5183.
- [5] M. Yaffe, J. A. Rowlands, *Phys. Med. Biol.* **1997**, *42*, 1.
- [6] F. Moretti, G. Patton, A. Belsky, M. Fasoli, A. Vedda, M. Trevisani, M. Bettinelli, C. Dujardin, *J. Phys. Chem. C* **2014**, *118*, 9670.
- [7] V. B. Mykhaylyk, H. Kraus, M. Saliba, *Mater. Horiz.* **2019**, *6*, 1740.
- [8] M. Spahn, *Nucl. Instrum. Methods Phys. Res., Sect. A* **2013**, *731*, 57.
- [9] F. Maddalena, L. Tjahjana, A. Xie, Arramel, S. Zeng, H. Wang, P. Coquet, W. Drozdowski, C. Dujardin, C. Dang, M. D. Birowosuto, *Crytals* **2019**, *9*, 88.
- [10] W. Wei, Y. Zhang, Q. Xu, H. Wei, Y. Fang, Q. Wang, Y. Deng, T. Li, A. Gruverman, L. Cao, J. Huang, *Nat. Photonics* **2017**, *11*, 315.
- [11] S. Yakunin, M. Sytnyk, D. Kriegner, S. Shrestha, M. Richter, G. J. Matt, H. Azimi, C. J. Brabec, J. Stangl, M. V. Kovalenko, W. Heiss, *Nat. Photonics* **2015**, *9*, 444.
- [12] H. Wei, Y. Fang, P. Mulligan, W. Chuirazzi, H.-H. Fang, C. Wang, B. R. Ecker, Y. Gao, M. A. Loi, L. Cao, J. Huang, *Nat. Photonics* **2016**, *10*, 333.
- [13] W. Pan, H. Wu, J. Luo, Z. Deng, C. Ge, C. Chen, X. Jiang, W.-J. Yin, G. Niu, L. Zhu, L. Yin, Y. Zhou, Q. Xie, X. Ke, M. Sui, J. Tang, *Nat. Photonics* **2017**, *11*, 726.
- [14] Y. C. Kim, K. H. Kim, D. Y. Son, D. N. Jeong, J. Y. Seo, Y. S. Choi, I. T. Han, S. Y. Lee, N. G. Park, *Nature* **2017**, *550*, 87.
- [15] S. Shrestha, R. Fischer, G. J. Matt, P. Feldner, T. Michel, A. Osvet, I. Levchuk, B. Merle, S. Golkar, H. Chen, S. F. Tedde, O. Schmidt, R. Hock, M. Rührig, M. Göken, W. Heiss, G. Anton, C. J. Brabec, *Nat. Photonics* **2017**, *11*, 436.
- [16] H. Wei, J. Huang, *Nat. Commun.* **2019**, *10*, 1066.
- [17] W. Pan, B. Yang, G. Niu, K. H. Xue, X. Du, L. Yin, M. Zhang, H. Wu, X. S. Miao, J. Tang, *Adv. Mater.* **2019**, *31*, 1904405.
- [18] J. Liu, B. Shabbir, C. Wang, T. Wan, Q. Ou, P. Yu, A. Tadich, X. Jiao, D. Chu, D. Qi, D. Li, R. Kan, Y. Huang, Y. Dong, J. Jasieniak, Y. Zhang, Q. Bao, *Adv. Mater.* **2019**, *31*, 1901644.
- [19] G. J. Matt, I. Levchuk, J. Knüttel, J. Dallmann, A. Osvet, M. Sytnyk, X. Tang, J. Elia, R. Hock, W. Heiss, C. J. Brabec, *Adv. Mater. Interfaces* **2020**, *7*, 1901575.
- [20] W. Mengesha, T. Taulbee, B. Rooney, J. Valentine, *IEEE Trans. Nucl. Sci.* **1998**, *45*, 456.
- [21] J. Xu, Y. Shi, J. Xie, F. Lei, M. Cinibulk, *J. Am. Ceram. Soc.* **2013**, *96*, 1930.
- [22] B. Yang, L. Yin, G. Niu, J. H. Yuan, K. H. Xue, Z. Tan, X. S. Miao, M. Niu, X. Du, H. Song, E. Lifshitz, J. Tang, *Adv. Mater.* **2019**, *31*, 1904711.
- [23] L. Lian, M. Zheng, W. Zhang, L. Yin, X. Du, P. Zhang, X. Zhang, J. Gao, D. Zhang, L. Gao, G. Niu, H. Song, R. Chen, X. Lan, J. Tang, J. Zhang, *Adv. Sci.* **2020**, *7*, 2000195.
- [24] R. Zhuang, X. Wang, W. Ma, Y. Wu, X. Chen, L. Tang, H. Zhu, J. Liu, L. Wu, W. Zhou, X. Liu, Y. Yang, *Nat. Photonics* **2019**, *13*, 602.
- [25] S. Fan, G. Wu, H. Zhang, Y. Yu, J. Qiu, G. Dong, *J. Mater. Chem. C* **2015**, *3*, 6725.
- [26] S. Y. Janbandhu, S. R. Munishwar, R. S. Gedam, *Appl. Surf. Sci.* **2018**, *449*, 221.
- [27] M. Xia, C. Liu, Z. Zhao, B. Ai, Q. Yin, J. Xie, J. Han, X. Zhao, *J. Non-Cryst. Solids* **2015**, *429*, 79.
- [28] N. O. Dantas, G. de Lima Fernandes, O. Baffa, J. A. Gómez, A. C. Almeida Silva, *Appl. Phys. Lett.* **2014**, *105*, 132410.
- [29] X. Di, Z. Hu, J. Jiang, M. He, L. Zhou, W. Xiang, X. Liang, *Chem. Commun.* **2017**, *53*, 11068.
- [30] S. Liu, M. He, X. Di, P. Li, W. Xiang, X. Liang, *Ceram. Int.* **2018**, *44*, 4496.
- [31] B. Yang, F. Zheng, S. Mei, Z. Chen, Y. Xie, H. Dai, X. Wei, W. Zhang, F. Xie, J. Ju, Y. Chu, J. Zou, R. Guo, *Appl. Surf. Sci.* **2020**, *512*, 145655.
- [32] P. Li, Y. Duan, Y. Lu, A. Xiao, Z. Zeng, S. Xu, J. Zhang, *Nanoscale* **2020**, *12*, 6630.
- [33] Y. Cheng, C. Shen, L. Shen, W. Xiang, X. Liang, *ACS Appl. Mater. Interfaces* **2018**, *10*, 21434.
- [34] S. Liu, Y. Luo, M. He, X. Liang, W. Xiang, *J. Eur. Ceram. Soc.* **2018**, *38*, 1998.
- [35] B. Ai, C. Liu, J. Wang, J. Xie, J. Han, X. Zhao, J. Heo, *J. Am. Ceram. Soc.* **2016**, *99*, 2875.
- [36] S. Yuan, D. Chen, X. Li, J. Zhong, X. Xu, *ACS Appl. Mater. Interfaces* **2018**, *10*, 18918.
- [37] X. Huang, Q. Guo, D. Yang, X. Xiao, X. Liu, Z. Xia, F. Fan, J. Qiu, G. Dong, *Nat. Photonics* **2019**, *14*, 82.

- [38] Q. Hu, Z. Li, Z. Tan, H. Song, C. Ge, G. Niu, J. Han, J. Tang, *Adv. Opt. Mater.* **2018**, *6*, 1700864.
- [39] H. Yu, B. Zhang, X. Chen, X. Qian, D. Jiang, Q. Wu, J. Wang, J. Xu, L. Su, *Opt. Express* **2019**, *27*, 523.
- [40] D. Li, X. Zhang, L. Jin, D. J. O. e. Yang, *Opt. Express* **2010**, *18*, 27191.
- [41] L. Protesescu, S. Yakunin, M. I. Bodnarchuk, F. Krieg, R. Caputo, C. H. Hendon, R. X. Yang, A. Walsh, M. V. Kovalenko, *Nano Lett.* **2015**, *15*, 3692.
- [42] L. Gao, L. N. Quan, F. P. García de Arquer, Y. Zhao, R. Munir, A. Proppe, R. Quintero-Bermudez, C. Zou, Z. Yang, M. I. Saidaminov, O. Voznyy, S. Kinge, Z. Lu, S. O. Kelley, A. Amassian, J. Tang, E. H. Sargent, *Nat. Photonics* **2020**, *14*, 227.
- [43] R. Yuan, L. Shen, C. Shen, J. Liu, L. Zhou, W. Xiang, X. Liang, *Chem. Commun.* **2018**, *54*, 3395.
- [44] G. Pan, X. Bai, D. Yang, X. Chen, P. Jing, S. Qu, L. Zhang, D. Zhou, J. Zhu, W. Xu, B. Dong, H. Song, *Nano Lett.* **2017**, *17*, 8005.
- [45] R. Yuan, J. Liu, H. Zhang, Z. Zhang, G. Shao, X. Liang, W. Xiang, *J. Am. Ceram. Soc.* **2018**, *101*, 4927.
- [46] T. Wang, X. Xu, D. Zhou, J. Qiu, X. Yu, *Mater. Res. Bull.* **2014**, *60*, 876.
- [47] T. Jiang, X. Yu, X. Xu, H. Yu, D. Zhou, J. Qiu, *Opt. Mater.* **2014**, *36*, 611.
- [48] C. Yang, J. Zhang, W. T. Peng, W. Sheng, D. Liu, P. S. Kuttipillai, M. Young, M. R. Donahue, B. G. Levine, B. Borhan, R. R. Lunt, *Sci. Rep.* **2018**, *8*, 16359.
- [49] M. Nikl, A. Yoshikawa, *Adv. Opt. Mater.* **2015**, *3*, 463.
- [50] J. Q. Grim, Q. Li, K. B. Ucer, A. Burger, G. A. Bizarri, W. W. Moses, R. T. Williams, *Phys. Status Solidi A* **2012**, *209*, 2421.
- [51] W. Huda, R. B. Abrahams, *AJR, Am. J. Roentgenol.* **2015**, *204*, W393.
- [52] E. Samei, M. J. Flynn, D. A. J. M. p. Reimann, *Med. Phys.* **1998**, *25*, 102.